Effects of Moisture Based Grain Boundary Passivation on Cell Performance and Ionic Migration in Organic-Inorganic Halide Perovskite Solar Cells

Md Nadim Ferdous Hoque[1], Rui He[2], Juliusz Warzywoda[3], Zhaoyang Fan[1]*

[1]Department of Electrical and Computer Engineering and Nano Tech Center, Texas Tech University, Lubbock, TX 79409, USA

[2]Department of Electrical and Computer Engineering, Texas Tech University, Lubbock, TX 79409, USA

[3]Materials Characterization Center, Whitacre College of Engineering, Texas Tech University, Lubbock, TX 79409, USA

(* Contact author: Zhaoyang.Fan@ttu.edu)

Keywords: Perovskite, Grain boundaries, Passivation, Scanning Kelvin probe microscopy, Contact potential difference, Conductive atomic force microscopy, Ion migration

Abstract

Due to the polycrystalline nature, grain boundaries (GBs) in hybrid perovskite thin films play critical roles in determining the charge collection efficiency of perovskite solar cells (PSCs), material stability and in particular the ion migration, considering its relatively soft ionic bonds with a low formation energy. Different GB passivation methods are being studied, and introducing PbI_2-rich phase at GBs in methylammonium lead iodide ($MAPbI_3$) has been found to be useful. In this study, combining macroscale measurements with tip based microscopic probing that includes scanning Kelvin probe microscopy for surface potential mapping and conductive atomic force microscopy for charge transport mapping, we revealed the effects of PbI_2-rich phase at GBs, which was introduced in moisture-assisted synthesis of $MAPbI_3$ thin films. It was found that PbI_2 passivation of GBs could change the surface potential and charge carrier screening, and significantly retard current conduction at the GB while enhancing conduction through the grain interior (GI). Inhibition of ion migration at GBs, as well as enhanced PSC device performance, is reported.

Introduction

With easy formation of polycrystalline films and demonstrated high power conversion efficiency of over 22%, organic–inorganic halide perovskite solar cells (PSCs) have attracted tremendous research interest.[1,2] The photovoltaic community is witnessing the rapid development of PSC technology toward its commercialization in a relatively short time period, either as stand-alone cells or through tandem structure formation with silicon or other suitable semiconductors.[3] This unprecedented progress in PSC could be attributed to their fundamental material properties such as high absorption coefficients, long carrier diffusion lengths, low exciton binding energies, being relatively immune to surface and grain boundary states, etc.[4] Nevertheless, to fully exploit the potential of PSCs, several challenges must be overcome, among which, hybrid perovskite material stability and PSC device stability are dominant problems,[5,6] such as J-V hysteresis,[7] defects generation,[8] photon[9] and thermal[10] enhanced ion migration,[11-13] and ion migration related degradation,[14] as well as the severe environmental sensitivity. The nature of these materials, relatively soft ionic solids with a low formation energy, offers merits of solution deposition processing, but results in their tendency for ion migration, defect generation and even decomposition. Progress has been made recently to address stability issues through various approaches.[15-19]

Polycrystalline nature of hybrid perovskite films renders their surface and grain boundaries (GBs) with important roles in determining the material and device stability and performance. Surprisingly, the state-of-the-art PSCs with record efficiencies do not have the largest grain size.[20] This could be understood by considering that the overall quality of solution-processed perovskite films should not be simply judged by their grain size, since the variation of synthesis conditions to control the grain size will unavoidably change other film properties. It has been known that GBs in methylammonium lead iodide ($MAPbI_3$) hybrid perovskites are intrinsically benign for charge carriers without generating deep states based on first-principle calculations,[21] while many experimental measurements have demonstrated the potential barrier and band bending across GBs that favor charge carrier collection.[22,23] However, these evidences do not suggest GBs in hybrid perovskites have no adverse effects. Grain dependent photovoltaic (PV) performances have been widely reported.[24,25] Photoluminescence (PL) studies have shown weaker PL intensity at GBs along with faster non-radiative decay.[26,27] In fact, due to the weak bonds in hybrid perovskites and particularly at GBs, it is hard to imagine GB surfaces that could have ideal lattice planes without deep states. Recombination paths might be easily generated at these locations due to small formation energy of defects. GBs could also easily facilitate ion migration,[28] as have been reported.[22,29] The current conduction difference between grain interior (GI) and GB has been widely reported.[22,23,30-33] Therefore, surface and GB passivation[34-39] have attracted much attention recently. In particular, PbI_2 phase present at GBs is believed to play a role in passivation, contributing to enhanced performance.[40-42] Even though moisture is a significant factor causing performance degradation of PSCs through hybrid perovskite material decomposition, synthesis of this same material in a controlled moisture environment by introducing wide bandgap PbI_2-rich phase at regions with the weakest bonds, i.e., GBs thus becomes a self-tuned method to repair and passivate these GBs.

Herein, combining macroscale measurements with atomic force microscopy (AFM) tip based microscopic probing that includes scanning Kelvin probe microscopy (SKPM) and conductive AFM (c-AFM) mapping, we report a systematic study of moisture-assisted synthesis of $MAPbI_3$ thin films with emphasis on how PbI_2 passivation of GBs could change the surface potential and charge carrier screening, current conduction contrast reversal at GB and GI, and particularly the inhibition of ion migration at GBs, as well as PSC device performance.

Results and Discussions

$MAPbI_3$ thin films were spin-coated on TiO_2/FTO substrates using anti-solvent method in a N_2 filled glovebox. To achieve PbI_2 passivation on GBs, post-coating annealing was carried out in an air filled box with controlled relative humidity (RH) to obtain four samples at RH of 5% (sample S1), 15% (sample S2), 30% (sample S3), and 45% (sample S4). A reference sample (S0) was annealed in the N_2 filled glovebox without passivation. The thickness of all samples was tuned to be similar in the range of ~400 nm. The morphologies of these samples, characterized by scanning electron microscopy (SEM) and atomic force microscopy (AFM), are presented in Figure S1 in the Supplementary Information (SI). Sample S3 has the largest average grain size of ~1.4 μm, while sample S1 has the smallest average grain size of 0.52 μm μm. Roughness of the samples was similar, as determined from the topographic AFM images, and varied from 14 nm to 24 nm, with sample S1 being the smoothest due to its smallest average grain size. The slight increase of roughness with grain size could be attributed to the small increase in GB width, as noticed from those images. Since the film thickness is only ~400 nm, the cross-sectional SEM images (Figure S1a′-e′) suggest that in samples with a large grain size, GBs mainly exist along the vertical direction but not in the lateral direction. This is particularly true for samples S0 and S3 (Figure 1b,b′,c,c′), two samples on which our studies will focus.

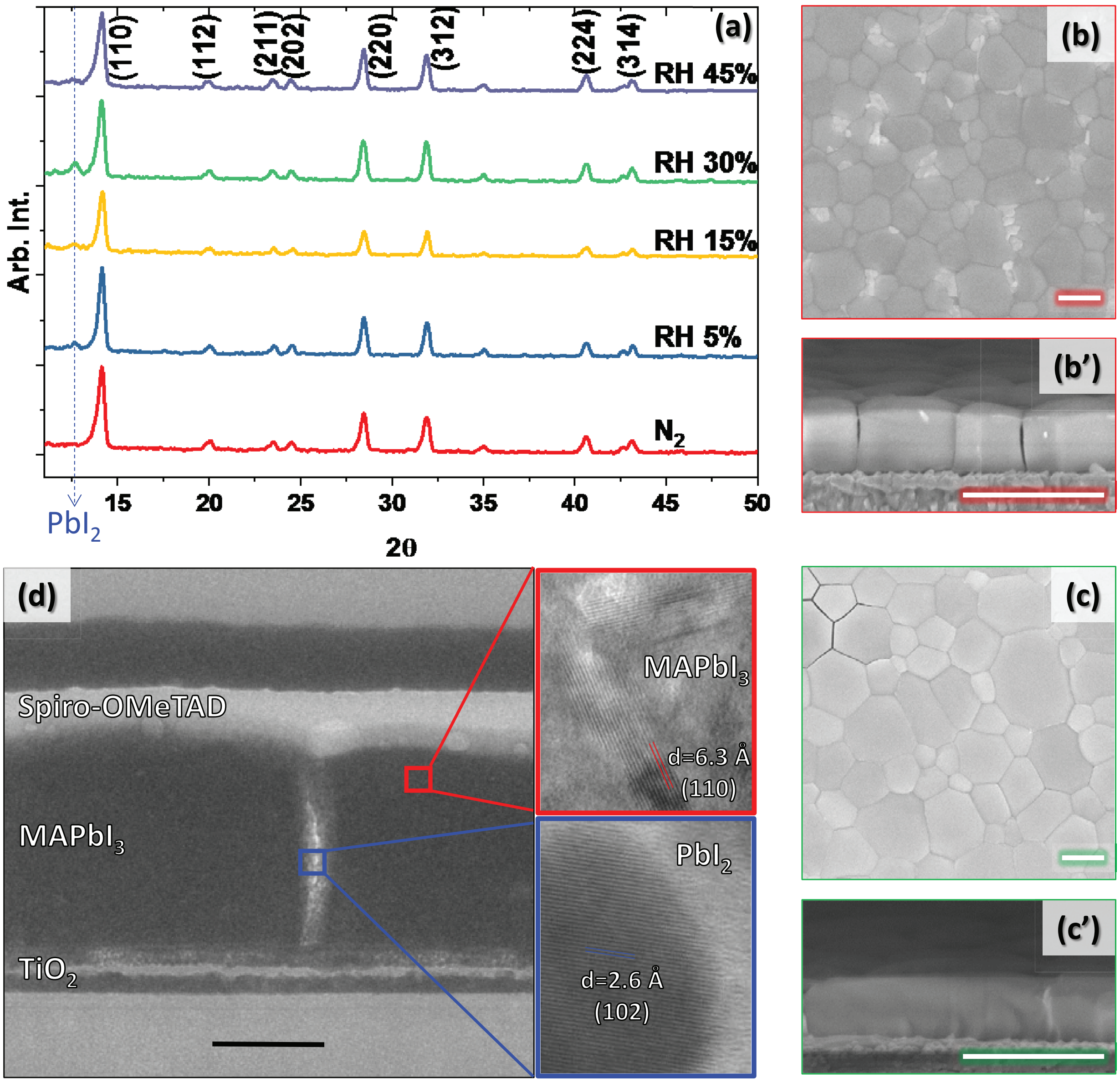

Figure 1. (a) XRD patterns of S0-S4 samples with the vertical line indicating PbI_2 *peak. SEM surface and cross section images for sample S0 (b,b') and S3 (c, c'). All scale bars in (b,b',c,c') represent 1 μm. (d) Cross section TEM image of a Spiro-MeOTAD/*$MAPbI_3/TiO_2/FTO$ *cell structure (sample S3),with a scale bar of 200 nm. The inset shows HRTEM image of the GI and the GB.*

In order to passivate the GBs, $MAPbI_3$ samples were fabricated in the presence of moisture. Composition of the resulting films was characterized using X-ray diffractometer (XRD), and is shown in Figure 1a. For all samples, the strongest diffraction peak was observed at ~14.1°. This peak is mainly due to diffraction from the (110) plane of the tetragonal phase $MAPbI_3$ lattice, but it also overlaps the peak due to diffraction from the (002) plane. However, only samples S1-S4 that were annealed in humid air, exhibited a weak but clearly identified peak at ~12.6°, which corresponds to the diffraction angle of PbI_2 (001) lattice plane. This suggests that a trace amount of PbI_2 was produced in the $MAPbI_3$ film for these samples, while such obvious trace amount of PbI_2, based on XRD measurement, was not observed for sample S0 annealed in N_2. Since moisture can solubilize and remove methylammonium from the perovskite lattice, it is anticipated that during the crystallization process of annealing, partial solvation of MAI occurs[43] leaving behind PbI_2-rich phase at GBs. This is confirmed by the transmission electron microscopy (TEM) study of the representative sample S3. As shown in Figure 1d, the GI exhibits a lattice spacing of 6.3 Å, in good agreement with the spacing of the (110) crystal planes of $MAPbI_3$, which produces the dominant XRD peak at ~14.1°. On the other hand, upon magnifying the GB area, it is clearly evident that PbI_2 is the dominant crystalline phase there, showing the (102) PbI_2 lattice plane with d-spacing of 2.6 Å, in agreement with other reports.[44]

The crystallinity and GB passivation of the perovskite film affects the solar cell performance. We therefore fabricated complete planar cells with a conventional structure of Au/Spiro-MeOTAD/$MAPbI_3$/TiO_2/FTO, where the $MAPbI_3$ layer was annealed in N_2 or humid air with different RH levels. Their performance was compared, and the results are shown in Figure S2 and Table S1. For the reference sample S0 annealed in N_2, a power conversion efficiency (PCE) of 12.8% was obtained, while a PCE of 15.0% was obtained for sample S3 annealed at 30% RH.

The consistency of this result was tested on 30 cells obtained at both S0 and S3 annealing conditions, and the PCE distribution curves are shown in Figure S3. The normal distribution shows that the average PCE increased from 12.1% (for S0) to 14.6% (for S3), yielding an increase of ~20% in PCE. In particular, all cells annealed in humid air exhibited larger open circuit voltage (V_{OC}) than the reference cell. Below, we will compare the performances of sample S0 annealed in N_2 and sample S3 annealed at 30% RH that have similar grain size to elucidate the effects of GB passivation.

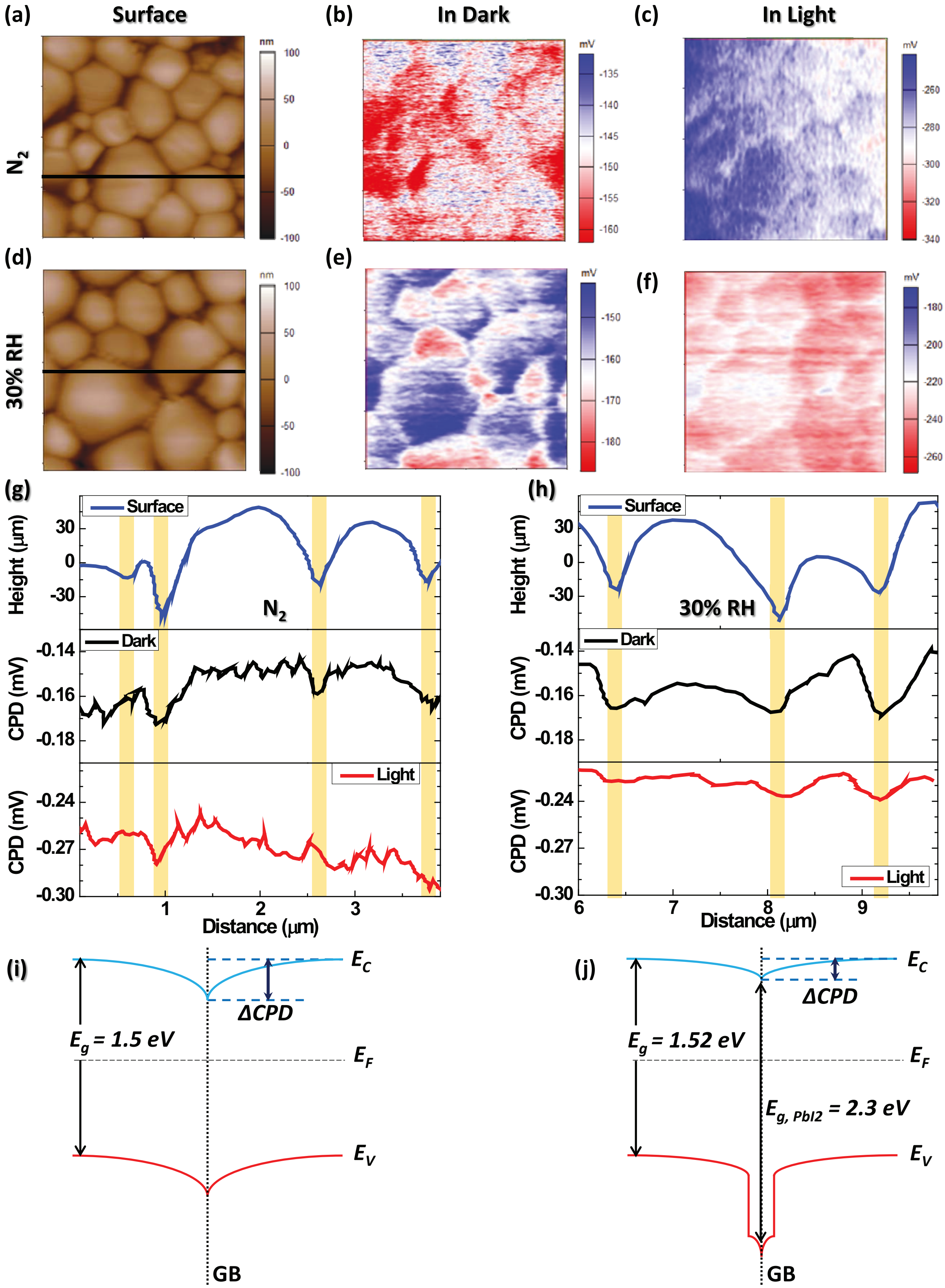
(a)
Surface
(b)
In Dark
(c)
In Light
N$_2$
nm
100
50
0
-50
-100
mV
-135
-140
-145
-150
-155
-160
mV
-260
-280
-300
-320
-340
(d)
(e)
(f)
30% RH
nm
100
50
0
-50
-100
mV
-150
-160
-170
-180
mV
-180
-200
-220
-240
-260
(g)
Surface
Height (µm)
30
0
-30
N$_2$
Dark
CPD (mV)
-0.14
-0.16
-0.18
Light
CPD (mV)
-0.24
-0.27
-0.30
1
2
3
Distance (µm)
(h)
Surface
Height (µm)
30
0
-30
30% RH
Dark
CPD (mV)
-0.14
-0.16
-0.18
Light
CPD (mV)
-0.24
-0.27
-0.30
6
7
8
9
Distance (µm)
(i)
E_C
ΔCPD
E_g = 1.5 eV
E_F
E_V
GB
(j)
E_C
ΔCPD
E_g = 1.52 eV
E_F
$E_{g,\ PbI2}$ = 2.3 eV
E_V
GB

Figure 2. AFM surface and SKPM images under dark and light conditions for samples S0 (a-c) and S3 (d-f). Heights and CPD maps for samples S0 (g) and S3 (h). The corresponding line profiles were obtained along the indicated black line in (a) and (d). The highlighted regions in (g), and (h) indicate grain boundary area. Electronic band diagrams near GB for samples S0 (i) and S3 (j).

SKPM study was conducted to measure the contact potential difference (CPD) in order to understand the effects of GBs and the passivation by the PbI_2-rich phase at GBs. $MAPbI_3$ samples S0 and S3 were directly formed on FTO glass. Details of the SKPM measurement and the terminology are discussed in SI with illustrations in Figure S4. As shown by the AFM topography and CPD map in Figure 2, the CPD measured under dark condition exhibits clear contrast between GBs and GIs for both samples. Since measured CPD is the work function difference between the conductive AFM tip reference and the sample local surface, the change of measured CPD value reflects the variation in the work function of the sample local surface, and the brighter area with less negative CPD indicates the location with a higher work function. As illustrated in Figure S4, since the sample has a constant Fermi level across the grains, GBs with lower work function correspond to downward band bending. This downward band bending at GBs, attributed to the vacancies and interstitials present at the GB areas,[22] is generally considered beneficial for electron-hole pair separation and collection. It can be noted that there is inhomogeneity among neighboring grains regarding the potential value, especially in dark conditions for both samples, but under light with charge carrier generation, the sample surface shows more homogenous nature regarding this surface potential, in agreement with other reports.[45]

A line profile of topography and CPD map are compared for sample S0 and S3 in Figure 2g,h, in which GB areas are highlighted with vertical bars for easy identification. Sample S0 has a more non-uniform CPD profile inside the grain, compared to the CPD mapping of sample S3 that follows the surface more smoothly. It is also worth noting that few GB area shows opposite trend in CPD profile, especially for S0 (Fig. 2g), which probably occurs from the presence of other defects in the GB area with unbalanced charge state. Similar anomaly has been observed in previous reports as well.[22,45,46] However, for all the samples in both conditions there are clear differences between GB and GI as further shown in Figure S5. Histogram distribution of CPD of the two samples is shown in Figure S6, from which it is noticed that under dark condition, both S0 and S3 show similar valence band potential barriers at the GB, however, the distribution of the barrier has a maximum value of 43 meV for S0, while it is 52 meV for S3. This slight increase in barrier voltage is anticipated to be useful for charge screening, since the downward band bending helps electrons in flowing near the GB, while repelling and confining holes inside grains.[46] Under illumination with photocarriers filling the states, it is expected the barrier between GB and GI will be reduced so the surface potential becomes more uniform.[45] Several other works have reported the lowering of the potential barrier at the GB-GI interface upon illumination.[23,47] Indeed, for our case the best performing sample S3 showed the lowest potential barrier under illumination, enhancing the PV performance. From Figure S6, the distribution of the barrier under illumination has a maximum value of 77 meV for S0, while it is 42 meV for S3. This almost doubled increase is also translated in the higher V_{OC} value for S3 (0.95V for S0, while 1.02V for S3, Table S1). The difference in CPD distribution is further shown clearly in Figure S7.

To illustrate the possible effects of GB passivation and the resulting band bending on solar cell performances, energy band diagrams for samples S0 and S3 are schematically shown in Figure

2i, j, respectively. The measured bandgap of the S3 was slightly higher (1.52 eV) compared to the S0 (1.5 eV), as shown in Figure S8. For both samples GBs are darker with higher negative CPD than GIs, suggesting lower energy at GBs than GIs, and thus downward band bending at GBs. If we assume the bandgap of the S0 has no change at GBs, since PbI_2 has a wider bandgap of 2.3 eV, the band alignment and bending across the GB will be very different for the S0 and S3, as schematically shown. For the S0, the conduction and valence bands bend downward, caused by negative charge accumulation (I^- ion or electron trapping) at GBs, and the resulting potential barrier leads to hole depletion. In principle, such an electronic structure at GBs will enhance electron-hole pair separation and suppress the recombination loss; however, since the barrier is only a few tens of mV, its effect will be trivial, further considering that for large grains, the carrier lateral transport distance is longer than the vertical distance. As reported in the literature, GBs in $MAPbI_3$ show high charge carrier recombination rates. On the other hand, the band alignment across GBs in the S3 now will strongly screen positive ions to minimize GB current and ion migration, as will become clear in the following.

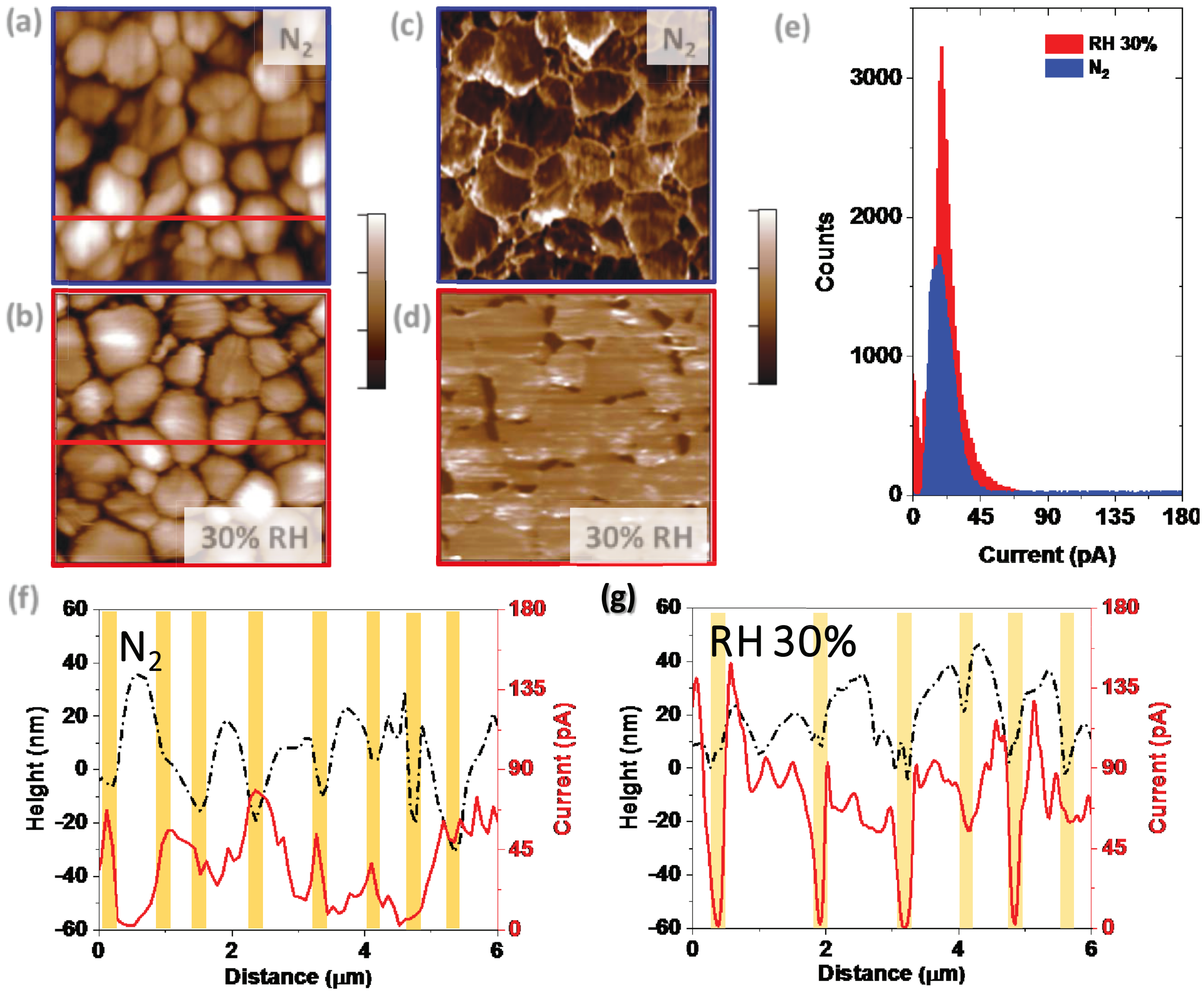

Figure 3. AFM surface images, and c-AFM images for (a,c) sample S0, and (b,d) sample S3. (e) Current distribution histograms obtained from (c), and (d). Heights and current for samples S0 in (f) and S3 in (g). The corresponding line profiles were obtained along the indicated red lines in (a) and (b). The highlighted regions in (f) and (g) indicates grain boundary area.

Further studies were conducted to map the current conduction across the surface using conductive AFM (c-AFM). The mapping was carried out in dark condition at 1.5 V to characterize the inherent material property in the absence of photon. As shown in Figures 3 and S9, for sample

S0, higher current appeared at the GB than at the GI. This was also observed for the sample prepared at 5% RH (S1). However, as the RH level for the sample preparation further increased, the current measured at the GI began to exceed that measured at the GB. The sample S3 showed the best contrast, where the GI exhibited higher current than the GB. In particular, whereas sample S0 showed less current in most areas with higher current near the trough areas indicating higher current on the GB, sample S3 exhibited more homogeneity having overall higher current in most areas with more current from the GI. From the current distribution histograms shown in Figure 3e, sample S3 exhibits higher current than sample S0 encompassing larger overall area, although the long blue tail indicates very large current measured at GB from S0. It is also noteworthy that the current distribution of sample S3 shows a second peak near <10 pA which is accounted for its GB area. This complete reversal in current conduction shows the importance of GB passivation. We speculate that the wide bandgap PbI_2 passivation at GBs screens away mobile ions, and thus minimizes the current conduction along GBs.

To reiterate this result, the line profiles have been compared for samples S0 and S3, as shown in Figure 3f, g. It can be clearly seen that for S0, the GB shows higher current than the GI. In fact, some areas of GI for this sample have the lowest current in the profile, making it very inefficient for charge transfer. It is speculated that GBs have more current due to ionic migration, since they act as highway for the ionic movement.[48] On the other hand, current flow in S3 clearly shows lowest current conduction through the GB compared to the GI. In fact, large portion of GB area in S3 shows negligible current of few pA, which is on the order of noise level of the instrument. This trend can be attributed to the GB passivation.[49] Such a contrasting passivation is very beneficial for effective charge transfer through the active layer.

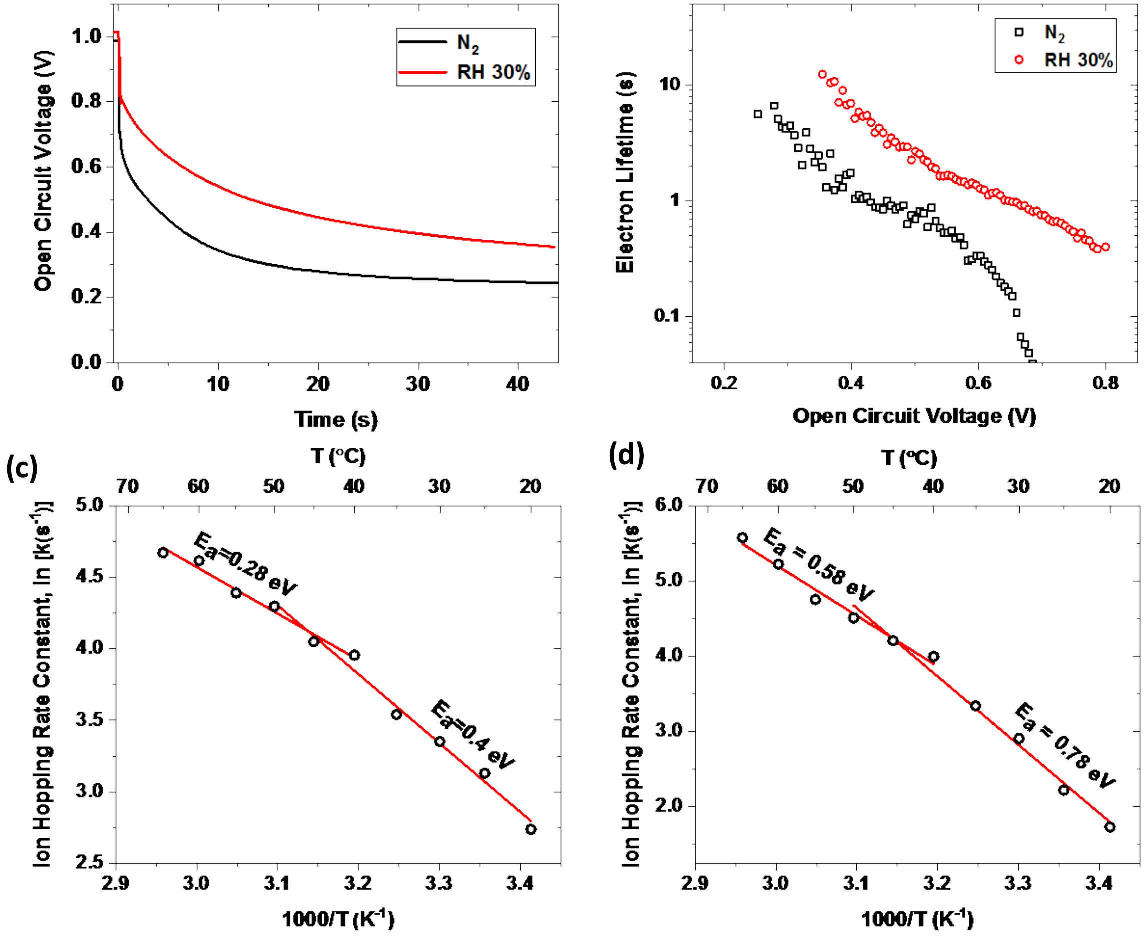

Figure 4. (a) Open circuit photovoltage decay (OCVD) measurement after the solar illumination is turned off at t=0s for samples S0 and S3. (b) Calculated electron recombination lifetime from the OCVD data. The Arrhenius plot of the ion hopping rate deduced from impedance spectroscopy data for samples S0 (c), and S3 (d).

We further took into account transport kinetics of different charge species to consolidate the passivation mechanism. The electron lifetime, which is related to the electron recombination kinetics, was determined via the open-circuit photovoltage decay (OCVD) method, which measures open circuit voltage (V_{oc}) decay immediately after switching off the solar illumination, as shown in Figure 4a. Then, the electron recombination lifetime τ_n was derived (Figure 4b) using the formula: $\tau_n = \frac{k_B T}{q}\left(\frac{dV_{OC}}{dt}\right)^{-1}$, where, k_B is the Boltzmann constant and T is the absolute temperature, which is selected as room temperature here. As the photovoltage decays faster for S0 compared to the S3 (0.244 V for the S0 vs. 0.355 V for the S3 at 43s after the light is turned off), the electron lifetime of the latter is longer than that of the former by more than one order of magnitude, e.g., 0.05s for the S0 compared to 0.85s for the S3 at 0.68 V.

One common issue for PSCs is the ion migration due to the soft bonds in hybrid perovskites, which contributes to the current mapping shown in Figure 3. As detailed in our previous studies,[13] ion hopping rates can be deduced from impedance spectroscopy. The Bode plots of the spectra for samples S0 and S3 are shown in Figure S10. Ion hopping rate constant is the inverse of relaxation time constant, which can be obtained from the low frequency peak in the Bode plot as explained in Figure S10. The activation energy of ion migration can be found from the Arrhenius plot of ion migration rate, as shown in Figure 4c,d. The $MAPbI_3$ goes through a phase transition from the low-temperature tetragonal phase to the high-temperature cubic phase. This phase change results in a difference in ion hopping activation energy and hence the two slopes observed intersect near 45 °C.[13] The derived activation energy for sample S0 is 0.28 eV and 0.4 eV for temperatures above and below 45 °C respectively, whereas the corresponding values for sample S3 are 0.58 eV and 0.78 eV. The higher activation energy in sample S3 reveals that ions need more energy for migration in this sample, thus passivating the ion channels, which are located mostly at the GBs, is effective in reduction of ion migration.[28] Using c-AFM, we probed the current conduction hysteresis at GI vs. GB for samples S0 and S3, as presented in Figure S11. C-AFM profile of the S0 shows that the GI exhibits negligible amount of hysteresis, whereas the GB shows significant hysteresis as well as higher current (e.g. 22 pA on GI vs 60 pA on GB at 2V). On the other hand, GB shows lesser hysteresis for the S3, and almost no hysteresis in the GI. The magnitude of the current is also significantly higher for the GI comparing to GB for the S3 (e.g. 25 pA on GI vs. 10 pA on GB at 2V).

Due to the relatively soft ionic bonds in hybrid perovskites that have a low formation energy, ion migration, particularly along the weakly bonded GB, is unavoidable. For stable PSCs, this phenomenon must be minimized, since the slow ion migration will screen the photo-voltage and thus reduce the achievable electronic current. From the SKPM measurement, we show how CPD changes at the GB for S0 (without passivation) and S3 (with passivation), and it is suggested that passivating the GB with Pb-rich phase will reduce the electron-hole recombination rate. As a result, a better overall current collection efficiency is achieved for S3 over S0. Using c-AFM, it is confirmed that ionic current is dominant through GBs in S0, which also works as a recombination center for electrons and holes, and overall GI current in S0 is thus reduced as well. In contrast, S3 shows higher ionic activation energy along with higher electron lifetime resulting in reduction of the current in GBs and increasing the current in GIs. Thus, all the indications from SKPM, c-AFM, and bulk electrical characteristics hold true as the passivation of GB helps in increasing the efficiency by ~20%.

Conclusion

In summary, $MAPbI_3$ thin films were synthesized with moisture assistance to introduce PbI_2-rich phase at GBs for passivation. Sample preparation in humid air at 30% RH resulted in the best PSC performance. Surface potential difference between GBs and GIs in the passivated and non-passivated samples, measured both in dark and under light illumination, was mapped using scanning Kelvin probe microscopy, and the results suggested the passivation effect of PbI_2-rich phase on charge screening and collection. This was further confirmed via c-AFM by the current mapping and conduction contrast between GBs and GIs for the passivated and non-passivated samples. Upon PbI_2 passivation, more current flows through GIs than GBs, whereas the opposite is observed for the non-passivated sample. The GB passivation further improved the electron lifetime, and in particular, reduced the ion migration rate with an enhanced ion migration activation energy. These results reveal the critical effects of PbI_2 minor phase introduced at GBs during moisture-assisted $MAPbI_3$ perovskite synthesis.

Experimental details

Device fabrication and material characterization

Complete planar cells were fabricated with a structure of FTO/TiO_2/$MAPbI_3$/HTM/Au. First, 50 nm compact TiO_2 layer was deposited on FTO coated glass; this was followed by annealing at 450 °C for 30 minutes. Afterwards, $MAPbI_3$ thin films were coated using anti-solvent method. Three different coating steps with speeds of 500, 3500, and 5000 rpm for 3, 10, and 30 seconds, respectively, were used. Four seconds before the start of the third step, 600 μL Toluene was dropped onto the film. $MAPbI_3$ coating was done in N_2 filled glovebox. The samples were subsequently annealed in a air-filled glovebox with a controlled relative humidity (RH) to obtain different samples at RH of 5% (sample S1), 15% (sample S2), 30% (sample S3), and 45% (sample S4). A reference sample (S0) was annealed in the N_2 filled glovebox. The thickness of all samples was tuned to be similar in the range of ~400 nm. The hole transport material (HTM), Spiro-MeOTAD mixed with 4-tert-butylpyridine and lithium bis(trifluoromethylsulphonyl)imide in acetonitrile, was then coated on $MAPbI_3$, which was followed by Au deposition. For AFM and impedance spectroscopy measurement, a simple sandwich structure of FTO/$MAPbI_3$/Au was used.

X-ray powder diffraction (XRD) analysis, scanning electron microscope (SEM) imaging, and UV-Vis-IR spectroscopy for absorbance measurement were carried out to compare quality/characteristic of different samples.

Focused ion beam (FIB), transmission electron microscope (TEM), and energy dispersive spectroscope (EDS) analyses

Focused ion & electron beam (FIB) system (Hitachi NB5000) was used to lift out and thin a lamella of the perovskite sample for transmission electron microscope (TEM), and energy dispersive spectroscope (EDS) analyses. Prior to lift out, protecting layers of C and W were deposited on the sample. The final thickness of the lamella was approximately 100 nm. TEM imaging was performed using a Hitachi H-9500 TEM at 300kV acceleration voltage.

Conductive atomic force microscopy (c-AFM), and scanning Kelvin probe microscopy (SKPM) characterization

Atomic force microscopy (AFM) was carried out using an Asylum Research MFP-3D-SA AFM. For c-AFM studies, a special dual gain ORCA probe holder (Asylum Research, sensitivity 1×10^{-6} A/V and 1×10^{-9} A/V) was used together with conductive Pt coated probe (2 N/m, 70 kHz, model: AC240TM-R3).

For the scanning Kelvin probe microscopy (SKPM) measurements, conductive probe (Ti/Ir coated, 2.8 N/m, 75 kHz, model: ASYELEC.01-R2) was used in a Nap mode imaging. In this dual mode AFM characterization, first, standard AC mode imaging in air was used to scan the topography of the sample surface. This is followed by retracing the probe so that the tip is raised over the surface and scanning the surface topography along the same lines/points while keeping the constant distance from the sample surface to measure the surface potential.

Electrical characterization

The current density-voltage (J-V) curves of different cells along with the OCVD data were measured using a Keithley 2400 SourceMeter under a simulated light source of one-sun AM 1.5G illumination (100 mW/cm^2). For ionic activation energy measurements, IS study was conducted using an electrochemical workstation (BioLogic). The measurements were performed in a range of 1 MHz to 100 mHz in a N_2 filled glovebox. To heat up the sample, a thermo-electric generator, controlled by a thermo-electric controller was used which was calibrated using thermometer with temperature accuracy of ± 1 °C.

Supporting Information

SEM and AFM of all samples, J-V characteristics, PCE distribution, band energy diagram of SKPM measurement, SKPM of all samples, Histogram distributions of CPD, Tauc plot, c-AFM of all samples, Bode plots, and c-AFM based local I-V.

ACKNOWLEDGMENTS

This work was supported by the National Science Foundation (CBET-1438681).

References

(1) Zhou, Y.; Zhu, K. Perovskite Solar Cells Shine in the "Valley of the Sun". *ACS Energy Lett.* **2016**, *1*, 64-67.

(2) Li, X.; Bi, D.; Yi, C.; Décoppet, J.-D.; Luo, J.; Zakeeruddin, S. M.; Hagfeldt, A.; Grätzel, M. A Vacuum Flash–assisted Solution Process for High-efficiency Large-area Perovskite Solar Cells. *Science* **2016**, *353*, 58-62.

(3) Williams, S. T.; Rajagopal, A.; Chueh, C.-C.; Jen, A. K.-Y. Current Challenges and Prospective Research for Upscaling Hybrid Provskite Photovoltaics. *J. Phys. Chem. Lett.* **2016**, *7*, 811-819.

(4) Brittman, S.; Adhyaksa, G. W. P.; Garnett, E. C. The Expanding World of Hybrid Perovskites: Materials Properties and Emerging applications. *MRS Commun.* **2015**, *5*, 7-26.

(5) Kim, H. S.; Seo, J. Y.; Park, N. G. Material and Device Stability in Perovskite Solar Cells. *ChemSusChem* **2016**, *9*, 2528-2540.

(6) Wang, D.; Wright, M.; Elumalai, N. K.; Uddin, A. Stability of Perovskite Solar Cells. *Sol. Energy Mater. Sol. Cells* **2016**, *147*, 255-275.

(7) Chen, B.; Yang, M.; Priya, S.; Zhu, K. Origin of JV Hysteresis in Perovskite Solar Cells. *J. Phys. Chem. Lett.* **2016**, *7*, 905-917.

(8) Ball, J. M.; Petrozza, A. Defects in Perovskite-halides and Their Effects in Solar Cells. *Nat. Energy* **2016**, *1*, 16149.

(9) Zhao, Y.; Zhou, W.; Zhou, X.; Liu, K.; Yu, D.; Zhao, Q. Quantification of Light-enhanced Ionic Transport in Lead Iodide Perovskite Thin Films and its Solar Cell Applications. *Light: Sci. Appl.* 2017, *6*, e16243.

(10) Hoque, M. N. F.; Yang, M.; Li, Z.; Islam, N.; Pan, X.; Zhu, K.; Fan, Z. Polarization and Dielectric Study of Methylammonium Lead Iodide Thin Film to Reveal its Nonferroelectric Nature under Solar Cell Operating Conditions. *ACS Energy Lett.* **2016**, *1*, 142-149.

(11) Bag, M.; Renna, L. A.; Adhikari, R.; Karak, S.; Liu, F.; Lahti, P. M.; Russell, T. P.; Tuominen, M. T.; Venkataraman, D. Kinetics of Ion Transport in Perovskite Active Layers and its Implications for Active Layer Stability. *J. Am. Chem. Soc.* **2015**, *137*, 13130–13137.

(12) Yang, T. Y.; Gregori, G.; Pellet, N.; Grätzel, M.; Maier, J. The Significance of Ion Conduction in a Hybrid Organic–Inorganic Lead-Iodide-Based Perovskite Photosensitizer. *Angew. Chem.* **2015**, *127*, 8016-8021.

(13) Hoque, M. N. F.; Islam, N.; Li, Z.; Ren, G.; Zhu, K.; Fan, Z. Ionic and Optical Properties of Methylammonium Lead Iodide Perovskite across the Tetragonal–Cubic Structural Phase Transition. *ChemSusChem* **2016**, *9*, 2692-2698.

(14) Besleaga, C.; Abramiuc, L. E.; Stancu, V.; Tomulescu, A. G.; Sima, M.; Trinca, L.; Plugaru, N.; Pintilie, L.; Nemnes, G. A.; Iliescu, M. Iodine Migration and Degradation of Perovskite Solar Cells Enhanced by Metallic Electrodes. *J. Phys. Chem. Lett.* **2016**, *7*, 5168-5175.

(15) Li, D.; Liao, P.; Shai, X.; Huang, W.; Liu, S.; Li, H.; Shen, Y.; Wang, M. Recent Progress on Stability Issues of Organic–inorganic Hybrid Lead Perovskite-based Solar Cells. *RSC Adv.* **2016**, *6*, 89356-89366.

(16) Da, P.; Zheng, G. Tailoring Interface of Lead-halide Perovskite Solar Cells. *Nano Res.*, **2017**, *10*, 1471-1497.

(17) Zhou, Y.; Zhou, Z.; Chen, M.; Zong, Y.; Huang, J.; Pang, S.; Padture, N. P. Doping and Alloying for Improved Perovskite Solar Cells. *J. Mater. Chem. A* **2016**, *4*, 17623-17635.

(18) Gong, J.; Guo, P.; Benjamin, S. E.; Van Patten, P. G.; Schaller, R. D.; Xu, T. Cation Engineering on Lead Iodide Perovskites for Stable and High-performance Photovoltaic Applications. *J. Energy Chem.* **2017**, *27*, 1017-1039.

(19) Zhou, P.; Fang, Z.; Zhou, W.; Qiao, Q.; Wang, M.; Chen, T.; Yang, S. Nonconjugated Polymer Poly (Vinylpyrrolidone) as an Efficient Interlayer Promoting Electron Transport for Perovskite Solar Cells. *ACS Appl. Mater. Interfaces* **2017**, *9*, 32957-32964.

(20) Yang, W. S.; Park, B.-W.; Jung, E. H.; Jeon, N. J.; Kim, Y. C.; Lee, D. U.; Shin, S. S.; Seo, J.; Kim, E. K.; Noh, J. H. Iodide Management in Formamidinium-lead-halide–based Perovskite Layers for Efficient Solar Cells. *Science* **2017**, *356*, 1376-1379.

(21) Yin, W. J.; Shi, T.; Yan, Y. Unique Properties of Halide Perovskites as Possible Origins of the Superior Solar Cell Performance. *Adv. Mater.* **2014**, *26*, 4653-4658.

(22) Yun, J. S.; Ho-Baillie, A.; Huang, S.; Woo, S. H.; Heo, Y.; Seidel, J.; Huang, F.; Cheng, Y.-B.; Green, M. A. Benefit of Grain Boundaries in Organic–inorganic Halide Planar Perovskite Solar Cells. *J. Phys. Chem. Lett.* **2015**, *6*, 875-880.

(23) Li, J.-J.; Ma, J.-Y.; Ge, Q.-Q.; Hu, J.-S.; Wang, D.; Wan, L.-J. Microscopic Investigation of Grain Boundaries in Organolead Halide Perovskite Solar Cells. *ACS Appl. Mater. Interfaces* **2015**, *7*, 28518-28523.

(24) Reid, O. G.; Yang, M.; Kopidakis, N.; Zhu, K.; Rumbles, G. Grain-Size-Limited Mobility in Methylammonium Lead Iodide Perovskite Thin Films. *ACS Energy Lett.* **2016**, *1*, 561-565.

(25) Nie, W.; Tsai, H.; Asadpour, R.; Blancon, J.-C.; Neukirch, A. J.; Gupta, G.; Crochet, J. J.; Chhowalla, M.; Tretiak, S.; Alam, M. A. High-efficiency Solution-processed Perovskite Solar Cells with Millimeter-scale Grains. *Science* **2015**, *347*, 522-525.

(26) Vorpahl, S. M.; Stranks, S. D.; Nagaoka, H.; Eperon, G. E.; Ziffer, M. E.; Snaith, H. J.; Ginger, D. S. Impact of Microstructure on Local Carrier Lifetime in Perovskite Solar Cells. *Science* **2015**, aaa5333.

(27) Eperon, G. E.; Moerman, D.; Ginger, D. S. Anticorrelation between Local Photoluminescence and Photocurrent Suggests Variability in Contact to Active Layer in Perovskite Solar Cells. *ACS Nano* **2016**, *10*, 10258-10266.

(28) Yun, J. S.; Seidel, J.; Kim, J.; Soufiani, A. M.; Huang, S.; Lau, J.; Jeon, N. J.; Seok, S. I.; Green, M. A.; Ho-Baillie, A. Critical Role of Grain Boundaries for Ion Migration in Formamidinium and Methylammonium Lead Halide Perovskite Solar Cells. *Adv. Energy Mater.* **2016**, *6*, 1600330.

(29) Shao, Y.; Fang, Y.; Li, T.; Wang, Q.; Dong, Q.; Deng, Y.; Yuan, Y.; Wei, H.; Wang, M.; Gruverman, A. Grain Boundary Dominated Ion Migration in Polycrystalline Organic–inorganic Halide Perovskite Films. *Energy Environ. Sci.* **2016**, *9*, 1752-1759.

(30) Lee, B.; Lee, S.; Cho, D.; Kim, J.; Hwang, T.; Kim, K. H.; Hong, S.; Moon, T.; Park, B. Evaluating the Optoelectronic Quality of Hybrid Perovskites by Conductive Atomic Force Microscopy with Noise Spectroscopy. *ACS Appl. Mater. Interfaces* **2016**, *8*, 30985-30991.

(31) Kutes, Y.; Zhou, Y.; Bosse, J. L.; Steffes, J.; Padture, N. P.; Huey, B. D. Mapping the Photoresponse of $CH_3NH_3PbI_3$ Hybrid Perovskite Thin Films at the Nanoscale. *Nano Lett.* **2016**, *16*, 3434-3441.

(32) Son, D.-Y.; Lee, J.-W.; Choi, Y. J.; Jang, I.-H.; Lee, S.; Yoo, P. J.; Shin, H.; Ahn, N.; Choi, M.; Kim, D. Self-formed Grain Boundary Healing Layer for Highly Efficient $CH_3NH_3PbI_3$ perovskite solar cells. *Nat. Energy* **2016**, *1*, 16081.

(33) Ma, T.; Zhang, Q.; Tadaki, D.; Hirano-Iwata, A.; Niwano, M. Fabrication and Characterization of High-Quality Perovskite Films with Large Crystal Grains. *J. Phys. Chem. Lett.* **2017**, *8*, 720-726.

(34) Lee, D. S.; Yun, J. S.; Kim, J.; Soufiani, A. M.; Chen, S.; Cho, Y.; Deng, X.; Seidel, J.; Lim, S.; Huang, S. Passivation of Grain Boundaries by Phenethylammonium in Formamidinium-Methylammonium Lead Halide Perovskite Solar Cells. *ACS Energy Lett.* **2018**, *3*, 647-654.

(35) Jiang, L. L.; Wang, Z. K.; Li, M.; Zhang, C. C.; Ye, Q. Q.; Hu, K. H.; Lu, D. Z.; Fang, P. F.; Liao, L. S. Passivated Perovskite Crystallization via g-C_3N_4 for High-Performance Solar Cells. *Adv. Funct. Mater.* **2018**, *28*, 1705875.

(36) Fang, X.; Ding, J.; Yuan, N.; Sun, P.; Lv, M.; Ding, G.; Zhu, C. Graphene Quantum Dot Incorporated Perovskite Films: Passivating Grain Boundaries and Facilitating Electron Extraction. *Phys. Chem. Chem. Phys.* **2017**, *19*, 6057-6063.

(37) Zheng, Y.-Z.; Li, X.-T.; Zhao, E.-F.; Lv, X.-D.; Meng, F.-L.; Peng, C.; Lai, X.-S.; Huang, M.; Cao, G.; Tao, X. Hexamethylenetetramine-mediated Growth of Grain-boundary-passivation $CH_3NH_3PbI_3$ for Highly Reproducible and Stable Perovskite Solar Cells. *J. Power Sources* **2018**, *377*, 103-109.

(38) Jacobsson, T. J.; Correa-Baena, J.-P.; Halvani Anaraki, E.; Philippe, B.; Stranks, S. D.; Bouduban, M. E.; Tress, W.; Schenk, K.; Teuscher, J. l.; Moser, J.-E. Unreacted PbI_2 as a Double-edged Sword for Enhancing the Performance of Perovskite Solar Cells. *J. Am. Chem. Soc.* **2016**, *138*, 10331-10343.

(39) Shih, M.-C.; Li, S.-S.; Hsieh, C.-H.; Wang, Y.-C.; Yang, H.-D.; Chiu, Y.-P.; Chang, C.-S.; Chen, C.-W. Spatially Resolved Imaging on Photocarrier Generations and Band Alignments at Perovskite/PbI_2 Heterointerfaces of Perovskite Solar Cells by Light-Modulated Scanning Tunneling Microscopy. *Nano Lett.* **2017**, *17*, 1154-1160.

(40) Chen, Q.; Zhou, H.; Song, T.-B.; Luo, S.; Hong, Z.; Duan, H.-S.; Dou, L.; Liu, Y.; Yang, Y. Controllable Self-induced Passivation of Hybrid Lead Iodide Perovskites toward High Performance Solar Cells. *Nano Lett.* **2014**, *14*, 4158-4163.

(41) Zhang, T.; Guo, N.; Li, G.; Qian, X.; Zhao, Y. A Controllable Fabrication of Grain Boundary PbI_2 Nanoplates Passivated Lead Halide Perovskites for High Performance Solar Cells. *Nano Energy* **2016**, *26*, 50-56.

(42) Zhou, H.; Chen, Q.; Li, G.; Luo, S.; Song, T.-b.; Duan, H.-S.; Hong, Z.; You, J.; Liu, Y.; Yang, Y. Interface Engineering of Highly Efficient Perovskite Solar Cells. *Science* **2014**, *345*, 542-546.

(43) Eperon, G. E.; Habisreutinger, S. N.; Leijtens, T.; Bruijnaers, B. J.; van Franeker, J. J.; deQuilettes, D. W.; Pathak, S.; Sutton, R. J.; Grancini, G.; Ginger, D. S. The Importance of Moisture in Hybrid Lead Halide Perovskite Thin Film Fabrication. *ACS Nano* **2015**, *9*, 9380-9393.

(44) Du, T.; Burgess, C. H.; Kim, J.; Zhang, J.; Durrant, J. R.; McLachlan, M. A. Formation, Location and Beneficial Role of PbI_2 in Lead Halide Perovskite Solar Cells. *Sustainable Energy Fuels* **2017**, *1*, 119-126.

(45) Faraji, N.; Qin, C.; Matsushima, T.; Adachi, C.; Seidel, J. Grain Boundary Engineering of Halide Perovskite $CH_3NH_3PbI_3$ Solar Cells with Photochemically Active Additives. *J. Phys. Chem. C* **2018**, *122*, 4817-4821.

(46) Kim, D.; Kim, G. Y.; Ko, C.; Pae, S. R.; Lee, Y. S.; Gunawan, O.; Ogletree, D. F.; Jo, W.; Shin, B. Effects of Postsynthesis Thermal Conditions on Methylammonium Lead Halide Perovskite: Band Bending at Grain Boundaries and Its Impacts on Solar Cell Performance. *J. Phys. Chem. C* **2016**, *120*, 21330-21335.

(47) Edri, E.; Kirmayer, S.; Henning, A.; Mukhopadhyay, S.; Gartsman, K.; Rosenwaks, Y.; Hodes, G.; Cahen, D. Why Lead Methylammonium Tri-iodide Perovskite-based Solar Cells Require a Mesoporous Electron Transporting Scaffold (but not Necessarily a Hole Conductor). *Nano Lett.* **2014**, *14*, 1000-1004.

(48) Xing, J.; Wang, Q.; Dong, Q.; Yuan, Y.; Fang, Y.; Huang, J. Ultrafast Ion Migration in Hybrid Perovskite Polycrystalline Thin Films under Light and Suppression in Single Crystals. *Phys. Chem. Chem. Phys.* **2016**, *18*, 30484-30490.

(49) Ke, W.; Xiao, C.; Wang, C.; Saparov, B.; Duan, H. S.; Zhao, D.; Xiao, Z.; Schulz, P.; Harvey, S. P.; Liao, W. Employing Lead Thiocyanate Additive to Reduce the Hysteresis and Boost the Fill Factor of Planar Perovskite Solar Cells. *Adv. Mater.* **2016**, *28*, 5214-5221.

TOC

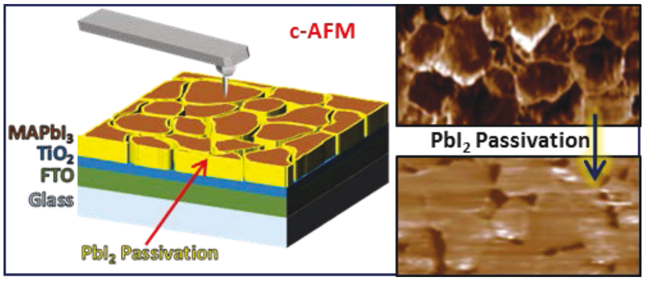
c-AFM
MAPbI$_3$
TiO$_2$
FTO
Glass
PbI$_2$ Passivation
PbI$_2$ Passivation

Supporting Information

Effects of Moisture Based Grain Boundary Passivation on Cell Performance and Ionic Migration in Organic-Inorganic Halide Perovskite Solar Cells

Md Nadim Ferdous Hoque[1], Rui He[2], Juliusz Warzywoda[3], Zhaoyang Fan[1*]

[1]Department of Electrical and Computer Engineering and Nano Tech Center, Texas Tech University, Lubbock, TX 79409, USA

[2]Department of Electrical and Computer Engineering, Texas Tech University, Lubbock, TX 79409, USA

[3]Materials Characterization Center, Whitacre College of Engineering, Texas Tech University, Lubbock, TX 79409, USA

(* Contact author: Zhaoyang.Fan@ttu.edu)

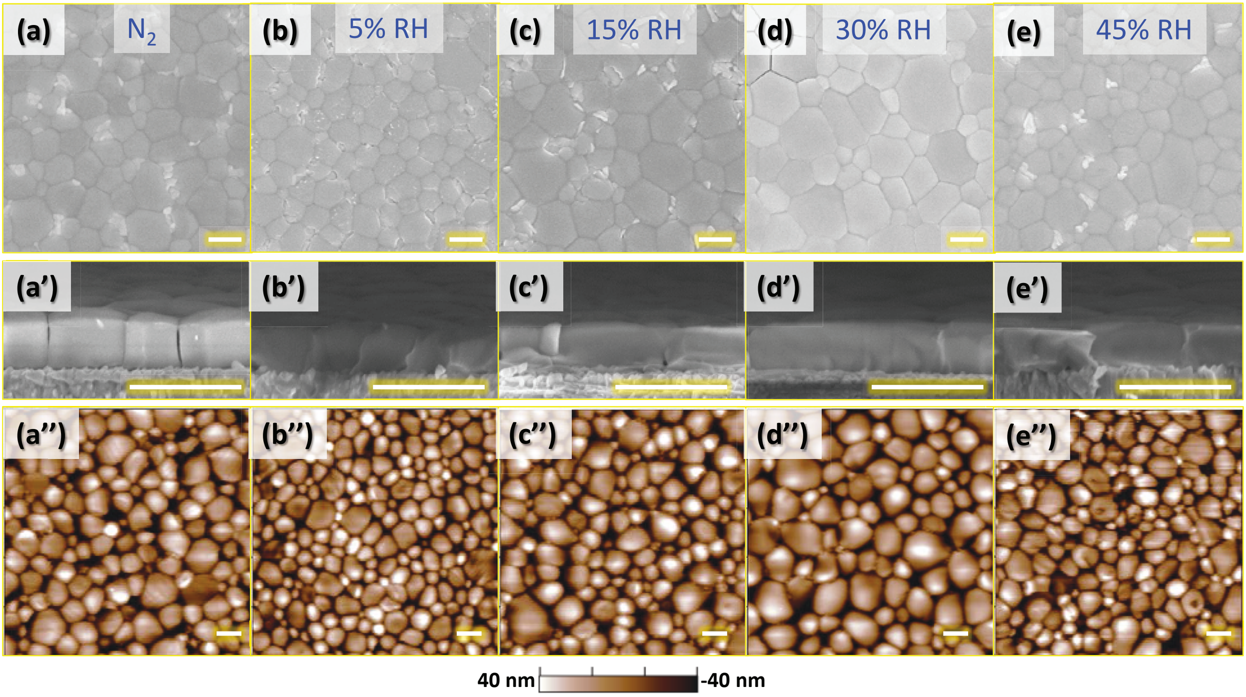

Figure S1. MAPbI$_3$ thin film fabricated at different conditions: (a-e) SEM surface images for samples S0, S1, S2, S3 and S4 respectively, (a'-e') SEM cross section images of the respective films, and (a''-e'') AFM topographic images for the corresponding films. All scale bars represent length of 1 µm.

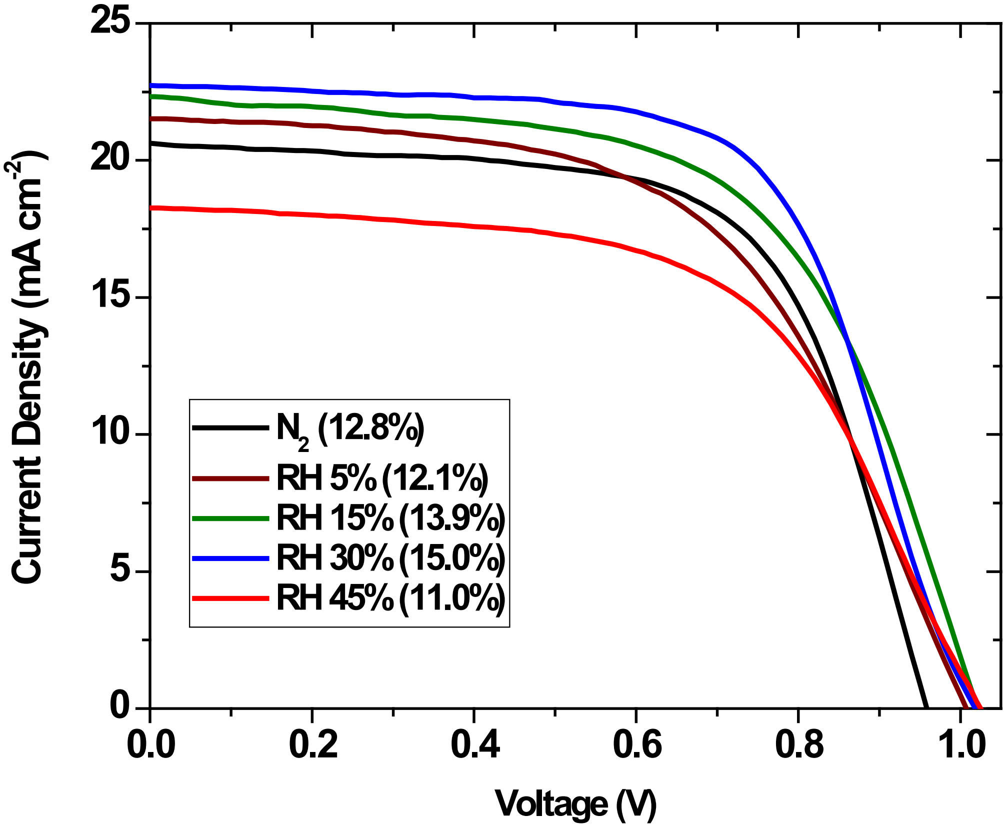

Figure S2. J-V curve comparison of the samples fabricated at different conditions under 1-sun with the indication of the PCE for champion devices in parenthesis.

Table S1. PSC Performance Comparison for Samples Prepared at Different Moisture Contents.

	J_{SC} (mA/cm^2)	**V_{OC}** (V)	**FF** (%)	**PCE_{MAX}** (%)	**R_S** (Ω-cm^2)	**R_{SH}** (Ω-cm^2)
S0	20.62	0.95	65	12.8	10.3	769
S1	21.53	1.00	56	12.1	14.5	833
S2	22.34	1.016	61	13.9	11.1	606
S3	22.74	1.02	65	15.0	10.1	994
S4	18.27	1.02	59	11.0	17.0	749

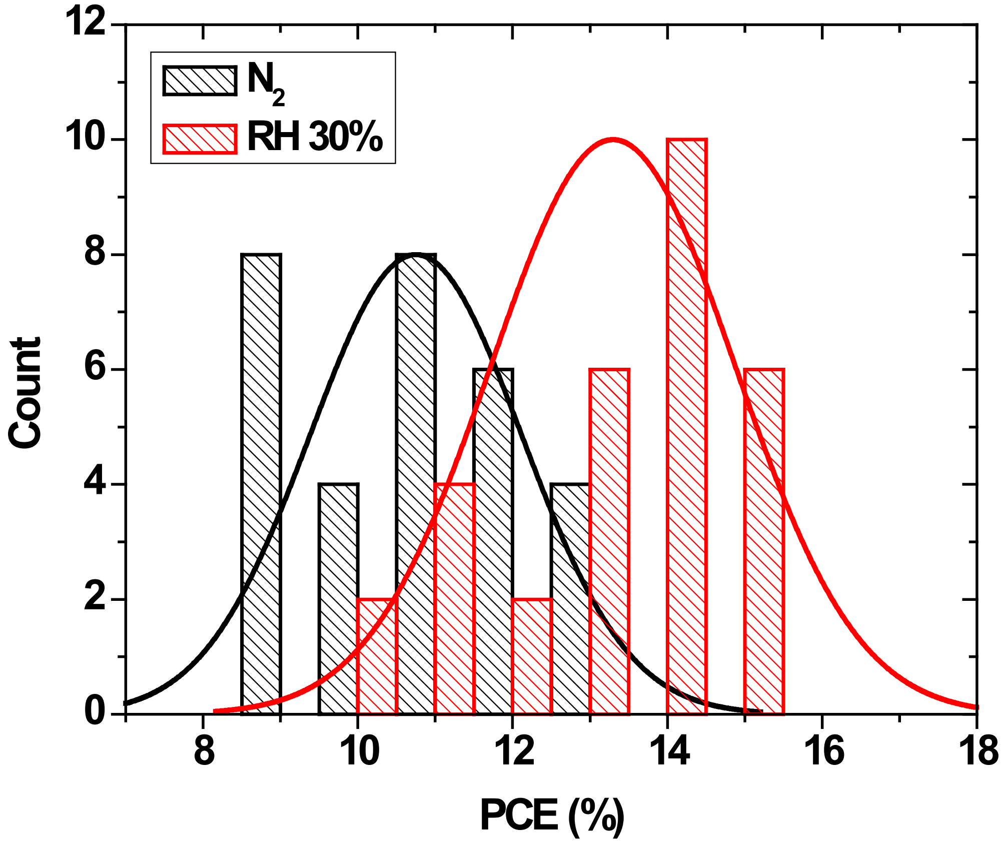

Figure S3. The PCE distribution histograms for samples prepared in N_2 and at 30% RH.

SKPM Measurement:

As shown in Figure S4, SKPM measured contact potential difference (V_{CPD}) or surface potential between the sample and the conductive tip, which can be calculated using the following formula,

$$V_{CPD} = \frac{q\varphi_{tip} - q\varphi_s}{-q} = \varphi_s - \varphi_{tip}$$

Where $q\varphi_{tip}$ is the work function of the tip and $q\varphi_s$ is the work function of the sample. For the SKPM experiment, ASYELEC.01-R2 conductive probes (Si coated with Ti/Ir (5nm/20nm)) from Asylum Research were used, which have a work function of 4.9 eV.

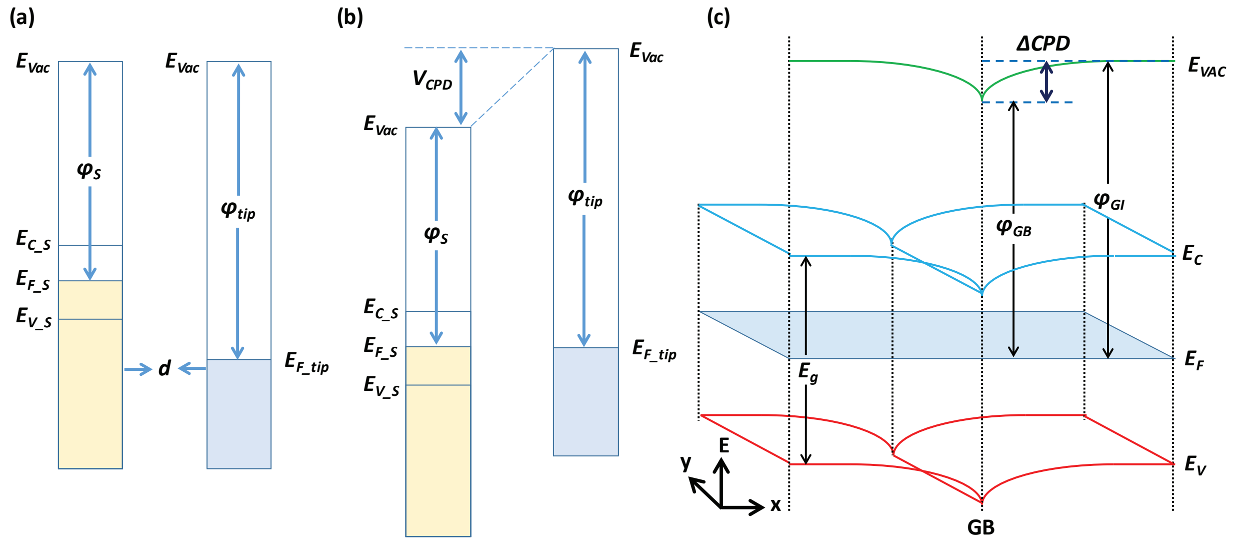

Figure S4. Band energy diagram of SKPM measurement between the sample and the tip. (a) With no electrical contact and being separated by distance d, sample and tip have different Fermi levels. (b) While in contact, the two Fermi levels will be aligned causing a potential difference called a contact potential difference (V_{CPD}). This amount of potential is applied during SKPM measurement to nullify the potential difference. (c) Electronic band diagram in two-dimensional space near a grain boundary (GB) area.

As an example, an arbitrary grain boundary band energy diagram is shown in Figure S4c. If the V_{CPD} value at grain boundary (GB) is - 0.2 V, it implies the work function, $q\varphi_{GB}$ value is 4.7 eV, while a V_{CPD} value of - 0.17 V at neighboring grain interior (GI) implies the work function, $q\varphi_{GI}$ value is 4.73 eV. This implies a downward band bending of 30 meV at the GB. It is noteworthy here that the $q\varphi_s$ value ~ 4.7 eV is almost in the middle of the conduction (3.9 eV) and valence (5.43 eV) bands of $MAPbI_3$ being an intrinsic semiconductor material.

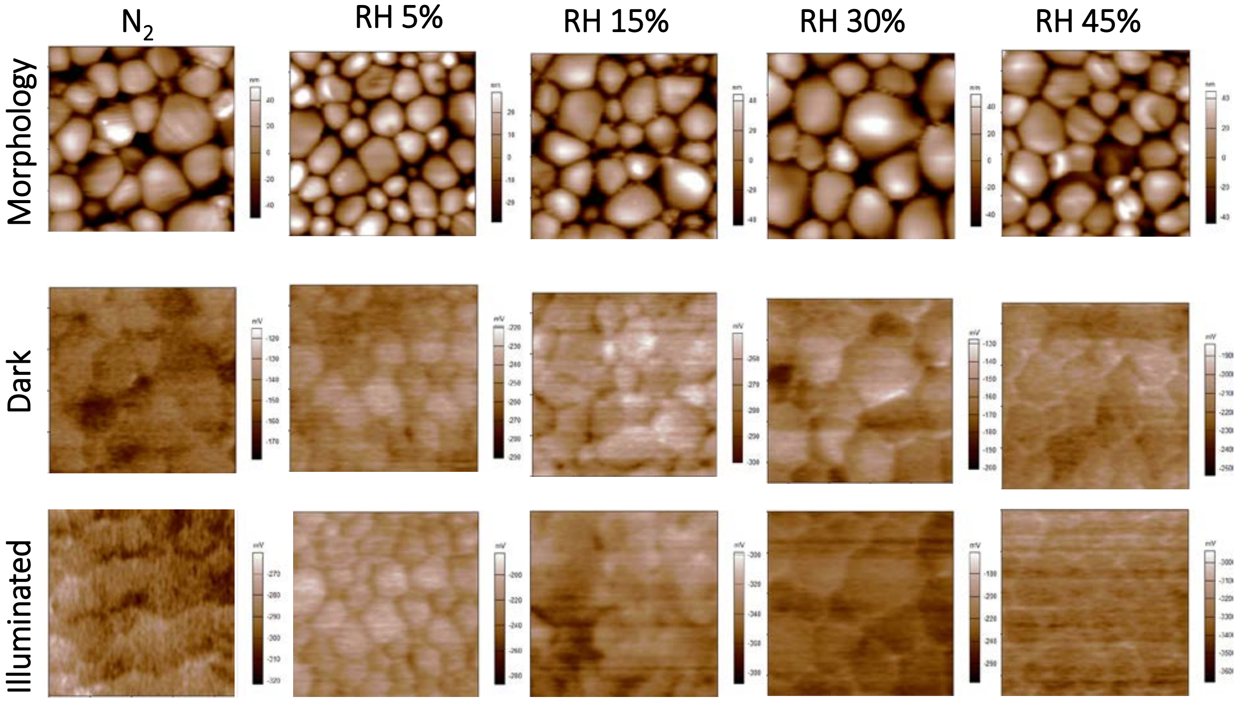

Figure S5. AFM surface and SKPM images of MAPbI₃/FTO samples prepared at different atmosphere under dark and light conditions.

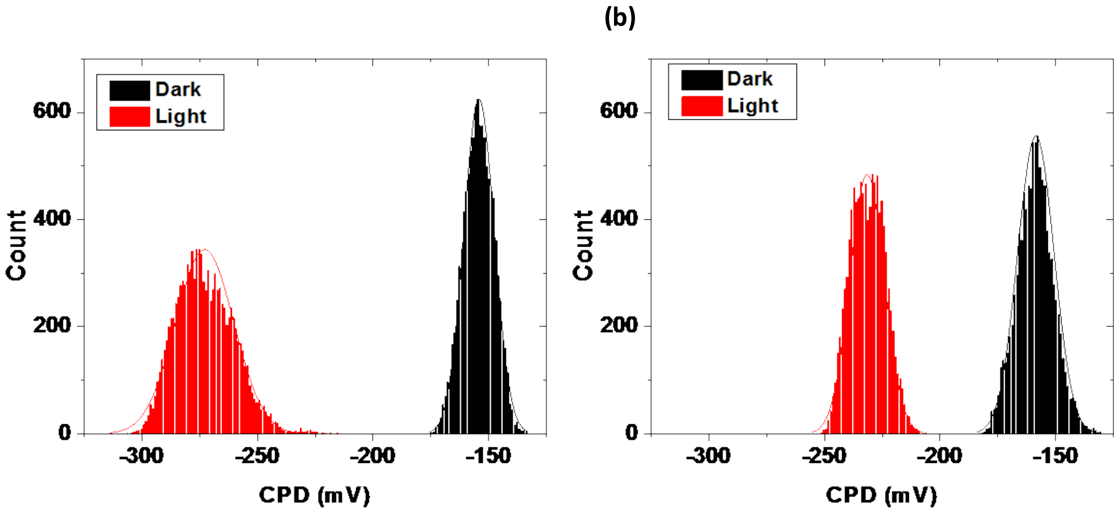

Figure S6. Histogram distributions of CPD for samples fabricated (a) in N_2 *ambient, and (b) at 30% RH, under dark and light conditions.*

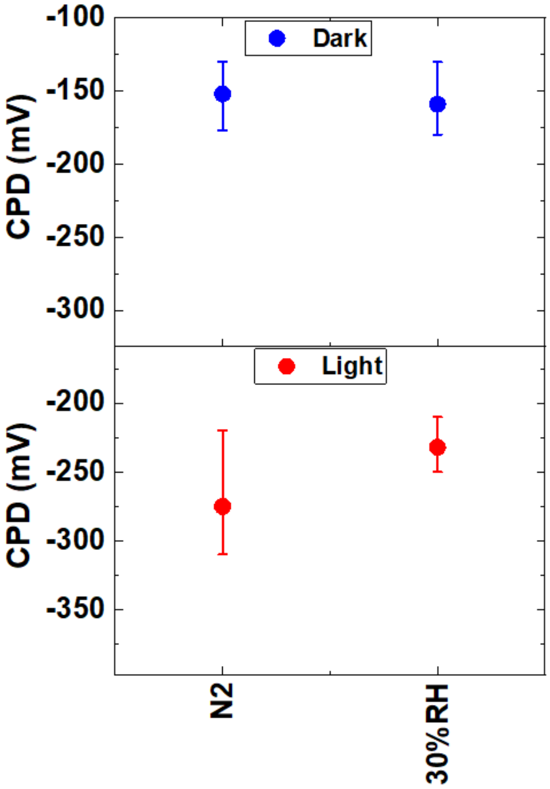

Figure S7. Contact potential difference (CPD) for samples fabricated in N_2*, and at 30% RH, under dark and light conditions. The average data have been obtained from Gaussian distribution, while the error bars represent the width of the distribution. Essentially, the length of the error bar represents average difference of CPD between grain boundary and grain interior.*

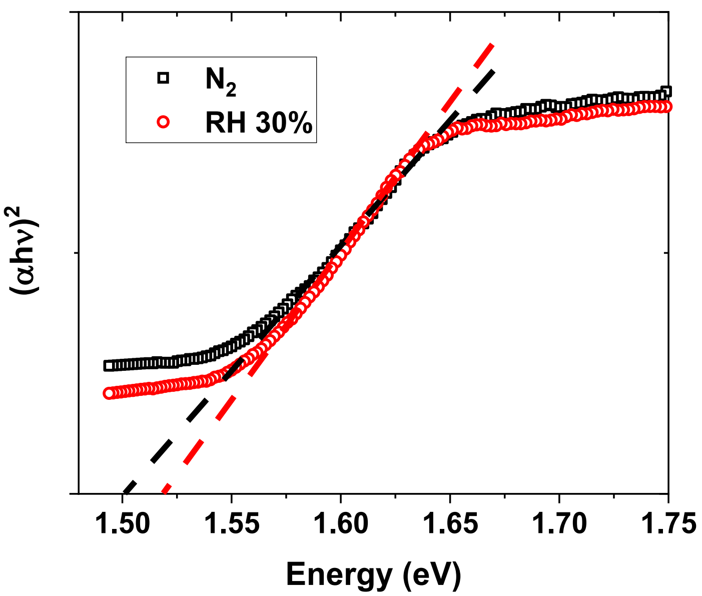

Figure S8. Tauc plot showing measured bandgap from absorbance spectra for samples prepared in N_2 *and at 30% RH.*

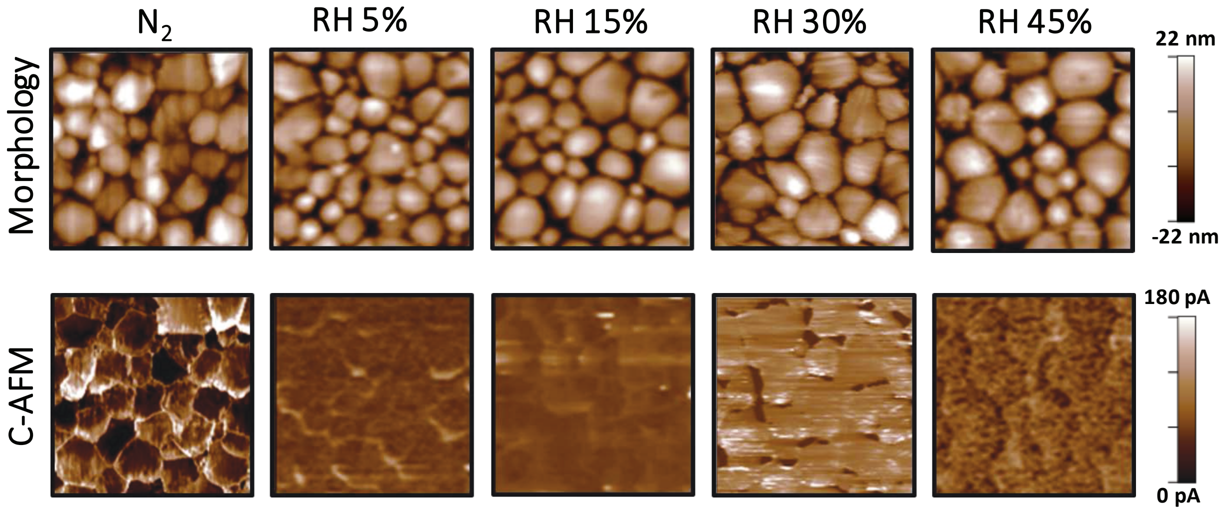

Figure S9. AFM surface and c-AFM images of $MAPbI_3$/FTO samples prepared at different atmosphere, measured under dark condition.

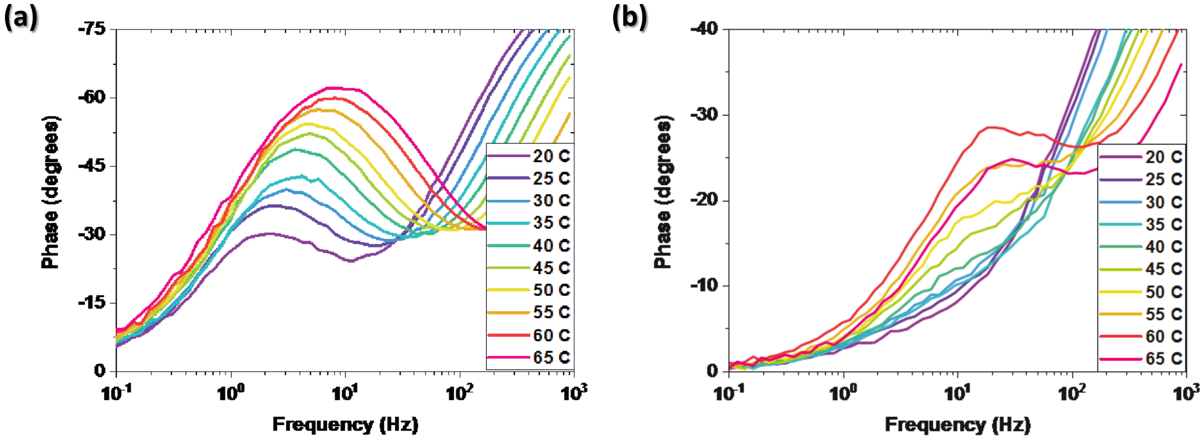

Figure S10. The Bode plots obtained from impedance spectroscopy data at different temperatures ranging from 20 to 65 °C to measure the ion hopping rate constant for (a) sample prepared in N_2, and (b) sample prepared at 30% RH.

The low frequency peaks from the Bode plot are result of ionic migration that happens at a much slower rate (on the order of several hundreds of ms) than electronic conduction. This low frequency peak (f_0), also known as relaxation frequency of ion hopping transportation, can be used to determine the relaxation time constant, τ, following the formula:

$$\tau = \frac{1}{2\pi f_0}$$

Finally, ion hopping rate constant, k can be determined by the following formula:

$$k = \frac{1}{\tau}$$

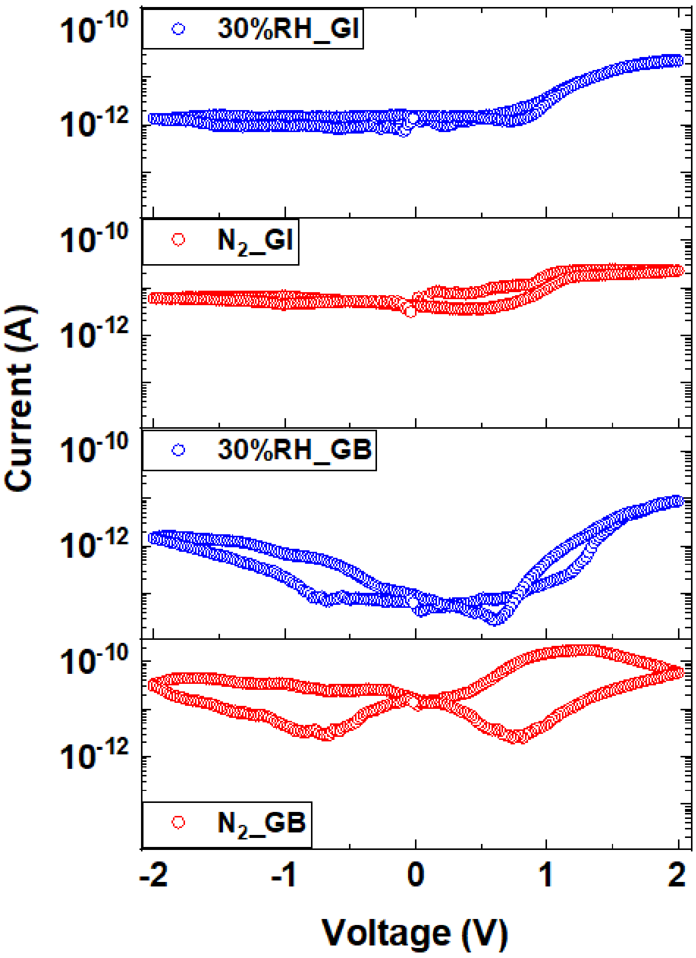

Figure S11. c-AFM based local dark current measured at the GI and the GB for samples S0 and S3 on surface of MAPbI$_3$*/FTO.*